Article:
Chen, L., Li, B. and de Borst, R. (2020) Adaptive isogeometric analysis for phase-field modeling of anisotropic brittle fracture. International Journal for Numerical Methods in Engineering, 121 (20). pp. 4630-4648. ISSN: 0029-5981

https://doi.org/10.1002/nme.6457

INTERNATIONAL JOURNAL FOR NUMERICAL METHODS IN ENGINEERING
Int. J. Numer. Meth. Engng 2018; **00**:1–20
Published online in Wiley Online Library (wileyonlinelibrary.com). DOI: 10.1002/nme

Adaptive isogeometric analysis for phase-field modelling of anisotropic brittle fracture

Lin Chen[1], Bin Li[2], René de Borst[1]*

[1]*University of Sheffield, Department of Civil and Structural Engineering, Sheffield S1 3JD, UK*
[2]*Cornell University, Sibley School of Mechanical and Aerospace Engineering, Ithaca, NY 14853, USA*

SUMMARY

The surface energy a phase-field approach to brittle fracture in anisotropic materials is also anisotropic and gives rise to second-order gradients in the phase field entering the energy functional. This necessitates C^1 continuity of the basis functions which are used to interpolate the phase field. The basis functions which are employed in IsoGeometric Analysis, such as Non-Uniform Rational B-Splines and T-Splines naturally possess a higher-order continuity and are therefore ideally suited for phase-field models which are equipped with an anisotropic surface energy. Moreover, the high accuracy of spline discretisations, also relative to their computational demand, significantly reduces the fineness of the required discretisation. This holds a fortiori if adaptivity is included. Herein, we present two adaptive refinement schemes in isogeometric analysis, namely, adaptive local refinement and adaptive hierarchical refinement, for phase-field simulations of anisotropic brittle fracture. The refinement is carried out using a subdivision operator and exploits the Bézier extraction operator. Illustrative examples are included which show that the method can simulate highly complex crack patterns such as zigzag crack propagation. An excellent agreement is obtained between the solutions from global refinement and adaptive refinement, with a reasonable reduction of the computational effort when using adaptivity. Copyright © 2018 John Wiley & Sons, Ltd.

Received . . .

KEY WORDS: Phase-field; anisotropic surface energy; isogeometric analysis; T-splines; adaptivity

1. INTRODUCTION

The numerical simulation of fracture is a technically relevant and scientifically challenging issue. Since the early simulations in the 1960s two parallel strands have been pursued, namely discrete and smeared methods [1]. While in the former approach cracks are treated as geometric discontinuities, leading to topological changes, see e.g. recent work which utilises spline technologies to model the discontinuity [2, 3, 4, 5], in the latter approach the discontinuity is modelled by distributing it over a small, but finite width [6]. The early attempts appeared to be deficient in the sense that they caused loss of well-posedness of the boundary value problem at, or close to structural failure. The concomitant grid sensitivity then prevents to obtain physically meaningful answers. While a host of solutions have been proposed to remedy this issue, gradient-enhanced damage models have proven to be particularly powerful for modelling fracture in quasi-brittle and ductile materials [7]. Recently, phase fields have been used to describe brittle fracture in an elegant and mathematically well-founded manner [8, 9, 10, 11]. Phase fields can be classified as a smeared approach, and bear much similarity to gradient-enhanced damage models [12].

*Correspondence to: R. de Borst, University of Sheffield, Department of Civil and Structural Engineering, Sheffield S1 3JD, UK. E-mail: r.deborst@sheffield.ac.uk

The phase-field approach to brittle fracture finds its origins in the so-called variational approach to fracture [8]. Herein, crack initiation and quasi-static propagation were considered as a minimisation problem of a Griffith-like energy functional. To make the problem amenable to large-scale computations a regularisation strategy was developed subsequently, which transforms the sharp crack into a distributed crack, which is governed by a phase-field variable c. The width of the distributed crack is set by an internal length scale ℓ_c [13]. The resulting functional contains first-order derivatives of the phase-field variable. This fits naturally in a standard $\mathcal{C}^0$ Galerkin approach, and therefore enables the use of standard finite element procedures.

In the vast majority of phase field models have been applied to the analysis of brittle fracture in materials with an isotropic surface energy, e.g. [13, 14, 15, 16]. Nevertheless, many natural and man-made materials have an anisotropic surface energy owing to their microstructure, for instance caused by the manufacturing process. This anisotropic character can significantly influence the crack path, for instance in single crystals, in geological materials, in rolled aluminium alloy plates, in fibre-reinforced composites, or in extruded polymers, e.g., [17, 18, 19].

Different from materials with an isotropic surface energy, higher-order gradients enter the functional which describes brittle fracture in materials with a strongly anisotropic surface energy [20, 21, 22, 23], inspired by the extended Cahn-Hilliard phase-field model proposed in the context of crystal growth and solidification. Preliminary numerical simulations [20], carried out using a meshfree discretisation method, appeared to well reproduce crack patterns observed experimentally [24].

Indeed, the presence of higher-order, in this case second-order derivatives of the phase-field variable in the resulting functional, requires a $\mathcal{C}^1$ interpolation of the phase field, which precludes the use of standard $\mathcal{C}^0$ finite elements. Next to the use of meshfree methods [20], mixed finite element formulations can be used to achieve $\mathcal{C}^1$ continuity, similar to formulations for plates and shells. Another, very natural approach is the use of B-spline technologies, as promulgated the past decade through IsoGeometric Analysis (IGA). B-splines, or to be more precise, Non-Uniform Rational B-Splines (NURBS) have been used before in the context of phase-field analyses of brittle fracture [25], but there the necessity to use a $\mathcal{C}^1$ approximation arose from the wish to use a spatial distribution for the phase field which is smooth at the centre of the phase field, rather than showing a kink as in most phase-field models for brittle fracture, e.g. [10, 11]. Herein, the expression for the surface energy which is dictated by the physics of (strongly) anisotropic brittle fracture is the sole motivation for the inclusion of higher-order terms, which necessitates the choice for a smooth interpolation of the phase-field variable.

Different from previous works which exploit IsoGeometric Analysis in the phase-field approach to brittle fracture, we use T-Splines as the basis functions. This has several advantages. To begin with, it allows us to pre-define the continuity of the basis functions during their construction [26]. Moreover, T-spline technology departs from the rigid tensor-product structure of NURBS and less control points are required when defining a complex geometry. In this contribution, we will further pursue these advantages and enhance them by using adaptivity, i.e. locally refined and hierarchical T-splines [27, 28]. Indeed, the higher accuracy provided by B-spline technology in general, combined with adaptivity facilitated by T-splines, can be important steps to make the phase-field approach to fracture practical, in the sense that the number of degrees of freedom remains reasonable also for bigger and more complex problems. Compatibility with standard finite element data structures is ensured through the use of Bézier extraction.

This contribution aims at developing an efficient and accurate solution strategy for distributed fracture modelling of materials that are governed by an anisotropic surface energy, see Section 2 for a succinct introduction to phase-field modelling of brittle fracture in such materials. As discussed, we have discretised the phase field using T-splines, and Section 3 gives a brief overview of the construction of the Bézier extraction operator and the subdivision operator for T-splines. In Section 4 we discuss the implementation of the adaptive local and hierarchical refinement. With that, all the necessary ingredients are in place to describe the algorithm for an element-based, adaptive isogeometric finite element method for higher-order phase models, and a range of examples show the versatility of the approach.

DOI: 10.1002/nme

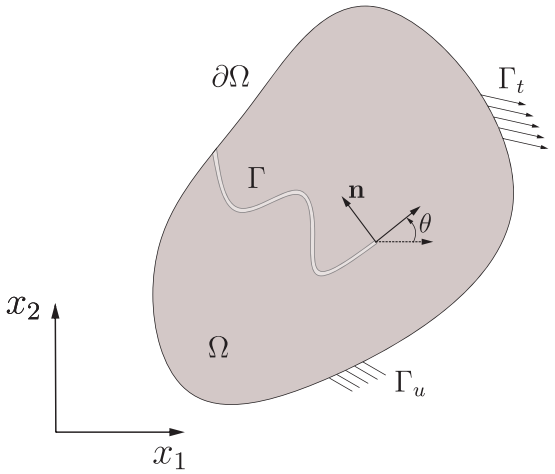

Figure 1. Two-dimensional crack Γ at an angle θ and with a unit vector $\boldsymbol{n}$ normal to the crack path.

2. PHASE-FIELD APPROXIMATIONS OF ANISOTROPIC FRACTURE

In the variational approach to fracture [8] crack initiation and quasi-static crack propagation are considered to be equivalent to the minimisation of a Griffith-like energy functional. Herein, we consider a cracked body $\Omega \subseteq \mathcal{R}^n$ with prescribed displacements $\hat{\mathbf{u}}$ on Γ_u and tractions $\hat{\mathbf{t}}$ on Γ_t. The total energy functional for the cracked body then reads:

$$\mathcal{E}(\mathbf{u}, \Gamma) = \int_{\Omega \setminus \Gamma} \mathcal{W}(\mathbf{u})\, d\Omega - \int_{\Gamma_t} \mathbf{u} \cdot \hat{\mathbf{t}}\, d\Gamma + \int_{\Gamma} \mathcal{G}_c(\boldsymbol{n})\, d\Gamma, \tag{1}$$

where the first term refers to the elastic energy stored in the cracked body, $\mathcal{W}(\mathbf{u})$ being the energy density function. We henceforth consider isotropic linear elasticity, i.e. $\mathcal{W}(\mathbf{u}) = \mu\, \boldsymbol{\varepsilon}(\mathbf{u}) \cdot \boldsymbol{\varepsilon}(\mathbf{u}) + \lambda/2\, \mathrm{tr}(\boldsymbol{\varepsilon}(\mathbf{u}))^2$ with $\boldsymbol{\varepsilon}$ the small-strain tensor, and λ and μ Lamé's constants. The second term is the potential energy of external forces, while the last term represents the (anisotropic) fracture surface energy in the sense of Griffith's theory of brittle fracture, and Γ is the discontinuity in the displacement field.

Materials with an anisotropic surface energy are characterised by an orientation-dependent fracture toughness $\mathcal{G}_c(\boldsymbol{n})$, where $\boldsymbol{n}$ is the unit vector normal to the crack surface, see Figure 1. In a two-dimensional setting, $\boldsymbol{n}$ can be replaced by an angle θ, and the surface energy can be parametrised as $G_c(\theta)$. In this study, the orientation-dependent fracture toughness is written as $\mathcal{G}_c(\mathbf{n}) = \mathcal{G}_0\, \gamma(\mathbf{n})$, where $\mathcal{G}_0$ is a scaling factor with the dimension of energy per unit surface and $\gamma(\mathbf{n})$ represents a dimensionless function of the normal vector $\boldsymbol{n}$. With this definition, Eq. (1) can be transformed into:

$$\mathcal{E}(\mathbf{u}, \Gamma) = \int_{\Omega \setminus \Gamma} \mathcal{W}(\mathbf{u})\, d\Omega - \int_{\Gamma_t} \mathbf{u} \cdot \hat{\mathbf{t}}\, d\Gamma + \mathcal{G}_0 \int_{\Gamma} \gamma(\boldsymbol{n})\, d\Gamma, \tag{2}$$

Direct numerical implementation of Griffith's energy functional, Eq. (2), is challenging because of the unknown location of the displacement jump. To transform the discrete crack problem into a distributed or smeared model a regularisation strategy has been proposed [13]. In this framework, cracks are represented by a scalar phase-field variable c, which ranges from 1 (the completely broken state) to 0 (fully intact material, away from the centre of the crack), which varies smoothly over a band of finite width, see for instance Francfort and Marigo [8] for the energy functional of materials characterised by an isotropic or weakly anisotropic surface energy.

As argued in the Introduction, materials with a strongly anisotropic surface energy exist and are technically relevant. To introduce such a more general anisotropy in the phase-field approach to brittle fracture, higher-order tensors and higher-order derivatives of the phase-field variable must

DOI: 10.1002/nme

be included [20]. To make the variational approach to brittle fracture also amenable to large-scale computations under such requirements, the energy functional of Eq. (2), which is applicable to a discrete crack, is replaced by the functional [23]:

$$\mathcal{E}_\ell\left(\mathbf{u},c\right)=\int_\Omega a(c)\mathcal{W}(\mathbf{u})\,d\Omega-\int_{\Gamma_t}\mathbf{u}\cdot\hat{\mathbf{t}}\,d\Gamma+\frac{\mathcal{G}_0}{\beta\ell_c}\int_\Omega\left(w(c)+\ell_c^4\,\nabla^2c:\mathbf{C}:\nabla^2c\right)\,d\Omega, \tag{3}$$

where $a(c)=(1-c)^2$ is a degradation function, $w(c)=9c$ is a monotonically increasing function which represents the energy dissipation per unit volume, and $\beta=4\int_0^1\sqrt{w(c)}\,dc=96/5$ is a normalisation parameter. ∇^2c is a Hessian, i.e. $(\nabla^2c)_{ij}=\frac{\partial^2c}{\partial x_i\partial x_j}$ and $\mathbf{C}$ is a positive-definite fourth-order tensor with the same symmetries as the linear elastic stiffness tensor [29]. Assuming a cubic symmetry, three material constants, C_{1111},C_{1122} and C_{1212}, suffice to define $\mathbf{C}$. The damage evolution then follows from (in a strong format) [20, 23]:

$$\frac{2\ell^4\mathcal{G}_0}{\beta}\left(2\left(C_{1122}+2C_{1212}\right)\frac{\partial^4c}{\partial x^2\partial y^2}+C_{1111}\left(\frac{\partial^4c}{\partial x^4}+\frac{\partial^4c}{\partial y^4}\right)\right)+\mathcal{W}(\mathbf{u})\,a'(c)\ell+\frac{\mathcal{G}_0}{\beta}w'(c)=0, \tag{4}$$

complemented by the irreversibility condition $\dot{c}\geq 0$. The resulting anisotropic surface energy $\mathcal{G}_c(\theta)$ then takes the form [20, 23]:

$$\mathcal{G}_c(\theta)=\mathcal{G}_0\sqrt[4]{C(\theta)}, \tag{5}$$

with

$$C(\theta)=\frac{1}{4}\left(3C_{1111}+C_{1122}+2C_{1212}\right)\left(1+\frac{C_{1111}-C_{1122}-2C_{1212}}{3C_{1111}+C_{1122}+2C_{1212}}\cos\theta\right). \tag{6}$$

Finally, an internal length scale $\ell_c>0$ has been introduced, which governs the width of the distributed crack. Typically, ℓ_c has a small value and several (Lagrangian) elements are needed to properly capture the strain profile over the crack width. This usually leads to very fine meshes with a concomitant computational burden. A significant advantage can thus be gained by using adaptive mesh refinement. Using Eq. (6) the effective internal length $\ell(\theta)$ then takes the form [20, 23]:

$$\ell(\theta)=\ell_c\sqrt[4]{C(\theta)}, \tag{7}$$

The optimal crack profile in a normal cross-section of the crack now reads [23]:

$$c(x)=1-\frac{3}{16}\frac{(x-x_0)^4}{\ell_c^4(\theta)}+\frac{|x-x_0|^3}{\ell_c^3(\theta)}-\frac{3}{2}\frac{(x-x_0)^2}{\ell_c^2(\theta)},\ x\in[x_0-D_0,x_0+D_0], \tag{8}$$

where $D_0=2\,\ell(\theta)=2\ell_c\sqrt[4]{C(\theta)}$ and the crack width is $2D_0$, see Figure 2(a). The surface energy is called weakly anisotropic if $\mathcal{G}_c(\theta)$ is convex and strongly anisotropic if $\mathcal{G}_c(\theta)$ is non-convex [20, 23]. The convexity can be checked graphically through the polar plot of the reciprocal surface energy $\mathcal{G}_c\left(\theta\right)$, see Figure 2(b).

Equation (4) is a fourth-order partial differential in the phase-field variable, which results in second-order spatial derivatives in the weak form. Clearly, $\mathcal{C}^1$ continuity is required for the interpolation of the phase-field variable. Indeed, the solution space, which is also used for the parameterisation of the geometry, should be constructed such that it allows for a higher-order continuous representation of the phase field. To accomplish this, T-splines are employed, which can produce higher-order continuous basis functions as well as exactly describe the geometry [27, 28]. There is a need to use fine discretisations, at least around the crack, in order to accommodate realistic values for the internal length scale ℓ_c. Therefore, it is desirable to locally refine the area near the crack path and adaptive refinement using T-splines is a powerful tool to achieve this. We will now describe how this can be done using local and hierarchical refinement of T-splines.

3. BÉZIER EXTRACTION OF REFINED T-SPLINES

We first review the concepts of Bézier extraction of locally refined T-splines [27, 30]. The Bézier extraction framework will be formulated such that it includes locally refined T-splines of a T-mesh,

DOI: 10.1002/nme

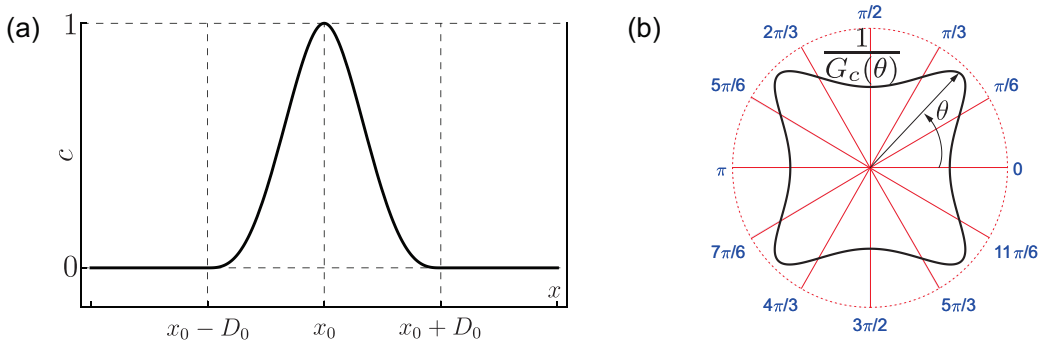

Figure 2. (a) Examples of the optimal crack profile $c(x)$ centered at x_0 for fully broken elastic bar. $2D_0$ is the crack width. (b) Polar plot of reciprocal anisotropic surface energy $\mathcal{G}_c(\theta)$.

which can be employed in adaptive isogeometric analysis. In the current contribution, we restrict the initial T-mesh to be a structured T-mesh with a nested spline space, such as a semi-standard T-spline mesh [27]. The same polynomial degree p is assumed in all parametric directions. A T-mesh $\mathcal{T}$ is composed of quadrilateral elements with T-junctions. Elements are defined as non-zero parametric areas which are confined by the edges of the T-mesh and the continuity reduction lines. An example of a quadratic T-spline mesh is given in Figure 3(a). In the figure, anchors are prescribed in the index and the parameter domains. For each anchor, a T-spline blending function N is defined by a local knot vector $\boldsymbol{\Xi}_i\,(i = 1, \cdots, n)$ with n the number of anchors on $\mathcal{T}$ [27]. A T-spline space $\mathcal{N} = \{N_i : \text{supp } N_i \in \mathcal{T}\}$ is constructed by the union of T-spline blending functions. A T-spline surface $\mathcal{S}\left(\xi^1, \xi^2\right)$ is described by anchors and blending functions:

$$\mathcal{S}\left(\xi^1, \xi^2\right) = \sum_{\alpha \in \mathcal{A}} \mathbf{P}_\alpha N_\alpha \left(\xi^1, \xi^2\right) \gamma_\alpha, \tag{9}$$

where $\mathcal{A}$ is the index set of anchors, $\mathbf{P}_\alpha$ denotes the coordinates of anchors, and γ_α the scaling weight, which enables the T-splines to satisfy the partition of unity property [27]. For completeness, we consider a rational T-spline surface, see Figure 3(a):

$$\mathcal{S}\left(\xi^1, \xi^2\right) = \sum_{\alpha \in A} \mathbf{P}_\alpha R_\alpha \left(\xi^1, \xi^2\right) \gamma_\alpha, \tag{10}$$

where $\mathbf{P}_\alpha = \left(x_\alpha^1, x_\alpha^2, w_\alpha\right)$ contains the coordinates of anchor α. w_α is the weight of anchor α. The weighted coordinates of anchor α are $\mathbf{P}_\alpha^w = \left(w_\alpha x_\alpha^1, w_\alpha x_\alpha^2, w_\alpha\right)$. $R_\alpha\left(\xi\right)$ denotes rational T-splines:

$$R_\alpha \left(\xi^1, \xi^2\right) = \frac{w_\alpha N_\alpha \left(\xi^1, \xi^2\right)}{W\left(\xi^1, \xi^2\right)} = \frac{w_\alpha N_\alpha \left(\xi^1, \xi^2\right)}{\sum_{\alpha \in A} w_\alpha N_\alpha \left(\xi^1, \xi^2\right)}. \tag{11}$$

We represent T-splines as element-wise Bernstein shape functions to directly incorporate it in standard finite element data structures [26]

$$\mathbf{N}_e \left(\xi^1, \xi^2\right) = \mathbf{C}_e \mathbf{B}_e \left(\xi^1, \xi^2\right), \tag{12}$$

with $\mathbf{C}_e$ the element Bézier extraction operator for anchors with support over element e.

For refinement we can also insert a meshline instead of inserting an anchor [26], see Figure 3(b). Generally, anchor insertions and meshline insertions are equivalent techniques for adaptive refinement [26]. In a T-mesh, a meshline ε must:

(i) not terminate in the centre of an element (knot span);
(ii) insert one line at a time;
(iii) span across at least $p + 2$ knots.

DOI: 10.1002/nme

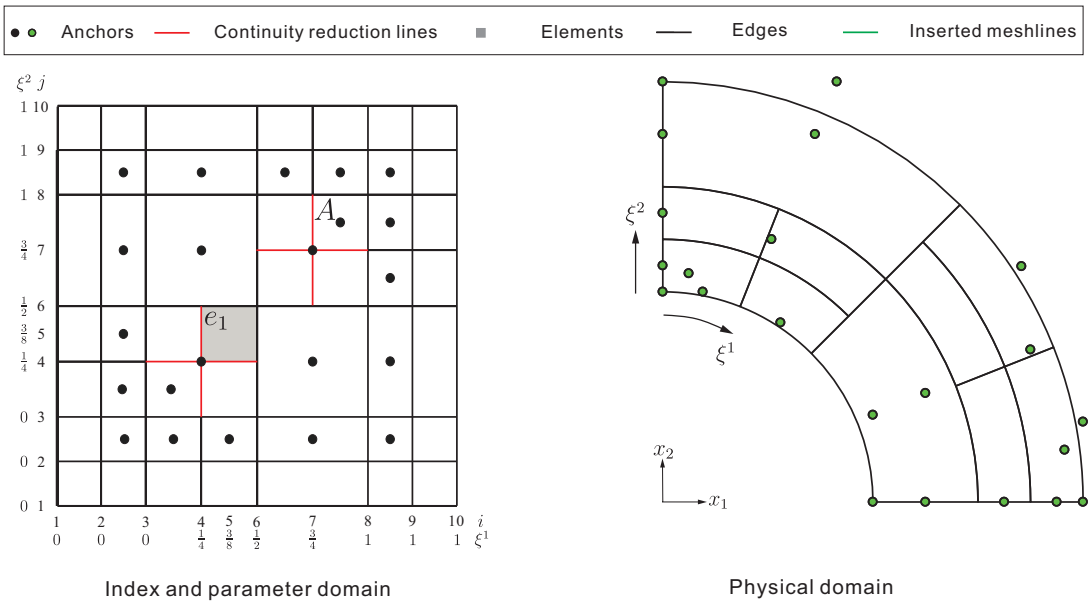

(a) Initial T-spline surface

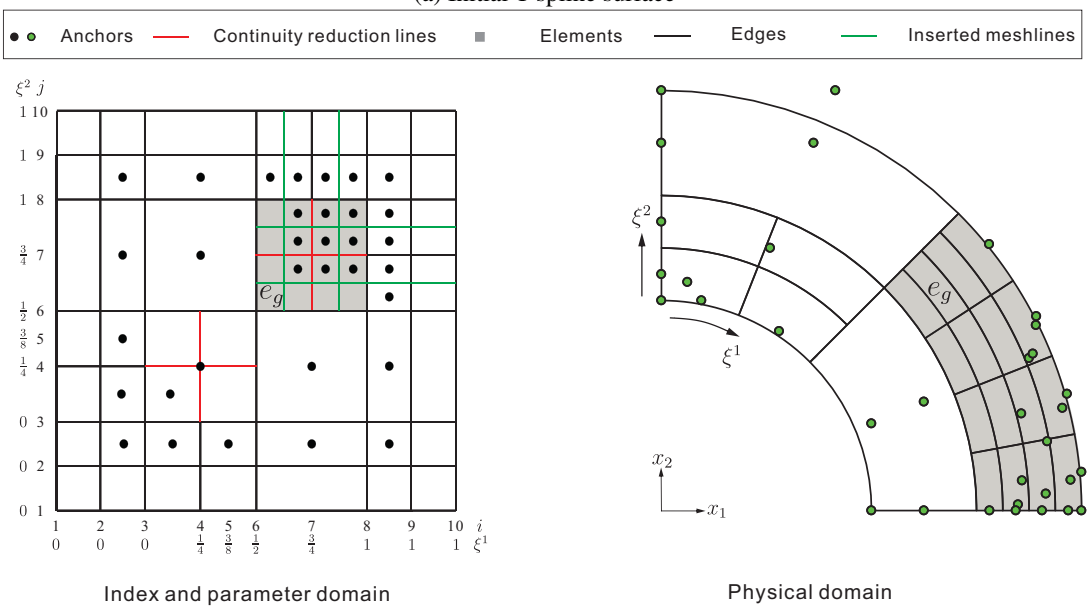

(b) Refined T-spline surface after meshline insertions

Figure 3. Example of a quadratic T-spline mesh. The object is given in the index domain $(i,\ j)$, in the physical domain $(x_1,\ x_2)$, and in the parameter domain $\left(\xi^1,\ \xi^2\right)$.

A meshline insertion can be either a new meshline, an elongation of an existing meshline, a joining of two existing meshlines, or increasing the multiplicity of an existing line [27].

Here we consider a T-mesh, $\mathcal{T}$, with n anchors, see Figure 3(a). Now, we insert a series of single meshlines, $\{\varepsilon_i\}_{i=1}^{n}$, in $\mathcal{T}$, which results in $\mathcal{T}_r$ with n_r anchors, see Figure 3(b). The T-splines $\mathcal{N}$ associated with $\mathcal{T}$ are now described by T-splines $\mathcal{N}_r$ associated with $\mathcal{T}_r$:

$$\mathbf{\Gamma N}\left(\xi^1,\ \xi^2\right) = \mathbf{\Gamma SN}_r\left(\xi^1,\ \xi^2\right) \tag{13}$$

DOI: 10.1002/nme

where $\mathbf{S}$ is the refinement operator, which is obtained by using the Bézier extraction, Equation (12) [27]. $\mathbf{\Gamma}$ denotes a diagonal matrix with the scaling weights γ of $\mathbf{N}$, and $\mathbf{N}$ and $\mathbf{N}_r$ are T-spline blending functions related to the T-mesh $\mathcal{T}$ and $\mathcal{T}_r$, respectively.

Considering Equation (13), the scaling weight γ^r of $\mathbf{N}_r$ is derived as:

$$\mathbf{\Upsilon}^r = \mathbf{\Upsilon}\mathbf{S} \quad \text{with} \quad \mathbf{\Upsilon}^r = \left[\gamma_1^r,\, \gamma_2^r,\, \cdots,\, \gamma_{n_r}^r\right] \quad \text{and} \quad \mathbf{\Upsilon} = \left[\gamma_1,\, \gamma_2,\, \cdots,\, \gamma_n\right] \tag{14}$$

with γ^r and γ are the scaling weights related to the T-mesh $\mathcal{T}_r$ and $\mathcal{T}$, respectively. The weighted coordinates of anchors on $\mathcal{T}_r$ are then derived as:

$$\mathbf{P}_r^w = \mathbf{\Gamma}_r^{-1}\mathbf{S}^{\mathrm{T}}\mathbf{\Gamma}\mathbf{P}^w \tag{15}$$

where $\mathbf{\Gamma}_r$ is a diagonal matrix with the scaling weight γ^r of $\mathbf{N}_r$ along the diagonal, see Equation (14). $\mathbf{P}^w$ and $\mathbf{P}_r^w$ are column vectors with the control points related to the T-meshes $\mathcal{T}$ and $\mathcal{T}_r$, respectively.

4. LOCAL AND HIERARCHICAL REFINEMENT USING BÉZIER EXTRACTION

The most common adaptive refinement techniques for T-splines are hierarchical refinement and local refinement (LR) by anchor insertions or meshline insertions in a T-mesh [31, 32]. These techniques are normally implemented using the sub-division approach. Herein, we will use Bézier extraction. First, some basic aspects of local and hierarchical refinement of T-splines are briefly summarised. Then, implementation aspects will be given for adaptive refinement on the basis of T-splines. Finally, the update of the state vector after adaptive refinement is given.

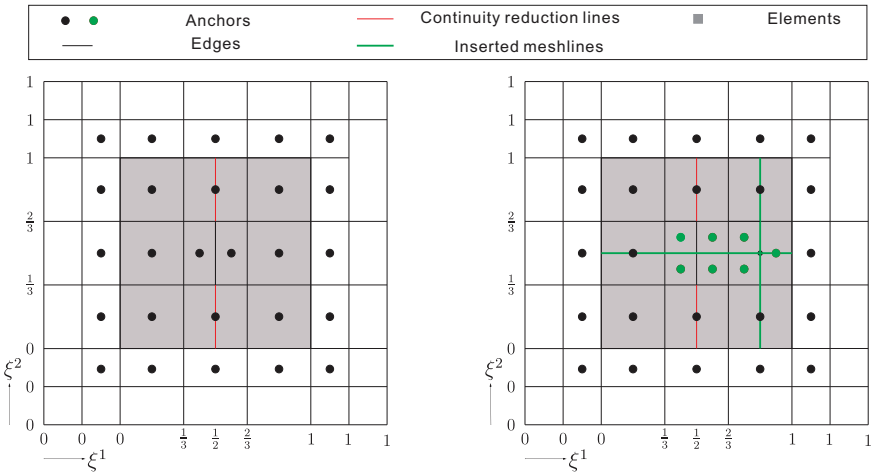

(a) initial T-mesh $\mathcal{T}_1$ (b) LR T-mesh $\mathcal{T}$

Figure 4. Example of a quadratic LR T-mesh in the parameter domain. The green lines indicate meshline insertions.

4.1. *Local refinement of T-splines in IGA*

We consider an initial T-mesh $\mathcal{T}_1$ with n anchors. Each anchor is associated with a local knot vector $\mathbf{\Xi}_i$ $(i = 1, \cdots, n)$ and a blending function $N_i\left(\xi^1, \xi^2\right)$. We suppose that a sequence of single meshlines $\{\varepsilon_i\}_{i=1}^n$ is inserted in $\mathcal{T}_1$, so that we obtain a nested Locally Refined T-mesh (LR T-mesh), $\mathcal{T}_n$, such that $\mathcal{T}_n \supset \mathcal{T}_{n-1} \supset \cdots \supset \mathcal{T}_2 \supset \mathcal{T}_1$, Figure 4. For the LR T-mesh $\mathcal{T}$, one can define LR T-spline blending functions N: $\mathbb{R}^2 \to \mathbb{R}$ if

- $N_{\mathbf{\Xi}}\left(\xi^1, \xi^2\right) = \gamma N_{\mathbf{\Xi}^1}\left(\xi^1\right) N_{\mathbf{\Xi}^2}\left(\xi^2\right)$ is a weighted blending function.

DOI: 10.1002/nme

- N has minimal support on $\mathcal{T}$, i.e. no other meshlines traverse the interior space of N.

An LR T-spline space $\mathcal{N} = \{N_i : \text{supp } N_i \in \mathcal{T}\}$ is defined by the union of LR T-spline functions.

The basic idea of LR T-splines is to maintain the minimal support after inserting meshlines into an LR T-mesh $\mathcal{T}$. This refinement is realised by knot insertions in each parametric direction. As an example we take a knot insertion in the ξ^1 parametric direction. We consider an LR T-spline blending function N_i which is defined by local knot vectors $\boldsymbol{\Xi}_i^1$ and $\boldsymbol{\Xi}_i^2$

$$\boldsymbol{\Xi}_i^1 = \left[\xi_1^1, \xi_2^1, \cdots, \xi_{i-1}^1, \quad \xi_i^1, \cdots, \xi_{p+1}^1, \xi_{p+2}^1\right]$$

and

$$\boldsymbol{\Xi}_i^2 = \left[\xi_1^2, \xi_2^2, \quad \cdots\cdots\cdots\cdots\cdots, \xi_{p+1}^2, \xi_{p+2}^2\right].$$

A new meshline, $\varepsilon = \hat{\xi} \times \left[\xi_1^2, \xi_{p+2}^2\right]$ is inserted in $\mathcal{T}$, yielding two additional local knot vectors: $\boldsymbol{\Xi}_{i1}^1$ and $\boldsymbol{\Xi}_{i2}^1$:

$$\begin{aligned} \boldsymbol{\Xi}_{i1}^1 &= \left[\xi_1^1, \xi_2^1, \cdots, \xi_{i-1}^1, \hat{\xi}, \xi_i^1, \cdots, \xi_{p+1}^1 \quad\right] \\ \boldsymbol{\Xi}_{i2}^1 &= \left[\quad \xi_2^1, \cdots, \xi_{i-1}^1, \hat{\xi}, \xi_i^1, \cdots, \xi_{p+1}^1, \xi_{p+2}^1\right] \end{aligned} \tag{16}$$

as well as two new anchors with respect local knot vectors $\boldsymbol{\Xi}_{i1}^1$ and $\boldsymbol{\Xi}_i^2$, $\boldsymbol{\Xi}_{i2}^1$ and $\boldsymbol{\Xi}_i^2$. Applying this refinement procedure to $\mathcal{T}$, we obtain updated anchors and elements on the refined LR T-mesh $\mathcal{T}_r$. The scaling weights and control points are then updated using Eqs (14) and (15).

Different refinement strategies have been proposed for LR T-splines [27, 33]: element based full span and minimal span refinement, blending function based structured mesh refinement, and element-based structured mesh refinement [26]. The starting point for all refinement strategies is that a certain element or blending function is marked for refinement. For instance, we consider the quadratic LR T-spline surface of Figure 3(a) as the initial LR T-spline surface. The element groups e_g are meant to be refined by the element-based structured mesh refinement strategy, see Figure 3(b). The implementation aspect of local refinement of T-splines is outlined in Section 4.3. In this contribution, the element-based structured mesh refinement strategy is employed.

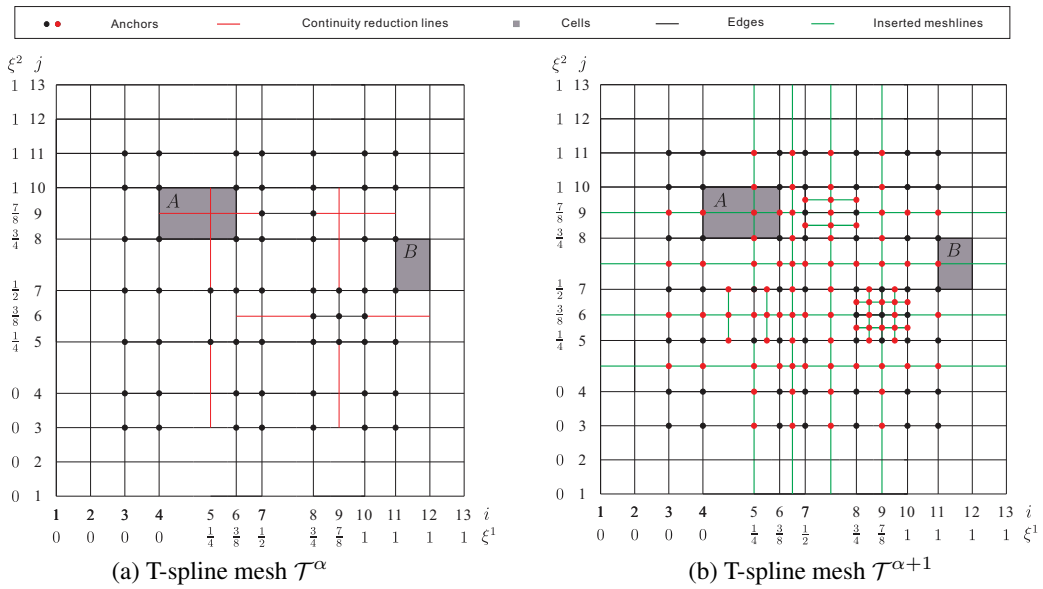

(a) T-spline mesh $\mathcal{T}^{\alpha}$ (b) T-spline mesh $\mathcal{T}^{\alpha+1}$

Figure 5. Construction of the cubic T-mesh $\mathcal{T}^{\alpha+1}$ from $\mathcal{T}^{\alpha}$. The anchors are indicated by circular dots. Black denotes the anchors on the T-spline mesh $\mathcal{T}^{\alpha}$, while red stands for those generated for the T-spline mesh $\mathcal{T}^{\alpha+1}$.

DOI: 10.1002/nme

4.2. Hierarchical refinement of T-splines in IGA

Hierarchical refinement was originally proposed for the adaptive refinement of a surface [34], but has subsequently also been used in analysis [2, 35]. Later, truncated hierarchical bases were proposed in [36]. To further improve the ability of hierarchical refinement, T-splines are considered as the input mesh [28, 32]. A hierarchical T-spline space is built on a finite sequence of $\mathfrak{L}$ nested T-spline spaces $\mathcal{N}^l$ bounded by $\mathfrak{L}$ parameter domains Ω^l, $l = 1, \cdots, \mathfrak{L}$. The nested nature of T-spline space defines the nested domains for the hierarchy:

$$\mathcal{N}^1 \subset \mathcal{N}^2 \subset \cdots \subset \mathcal{N}^{\mathfrak{L}} \qquad\qquad \Omega^{\mathfrak{L}} \subseteq \Omega^{L-1} \subseteq \cdots \subseteq \Omega^1. \tag{17}$$

To construct nested T-spline spaces $\mathcal{N}^\alpha \subset \mathcal{N}^{\alpha+1}$, $\alpha = 1, \cdots, \mathfrak{L}-1$, a multi-level T-spline mesh is constructed with a hierarchy of $\mathfrak{L}$ levels. In the multi-level mesh, the sequence of T-spline meshes $\mathcal{T}^{\alpha+1}$ is built by subdividing each effective rectangular cell in $\mathcal{T}^\alpha$ into two or four congruent cells by meshline insertions, where an effective rectangular cell is a cell with a non-zero parametric length in at least one parametric direction. Examples are the cells A and B in Figures 5(a) and 5(b). It is noted that, when defining the cells, the continuity reduction lines are not considered, Figure 5(b).

At each hierarchy level, we have n_i anchors with a corresponding local knot vector set $\mathbf{\Xi}_i = \left\{\Xi_i^j\right\}$ $(i = 1, 2, \ldots \mathfrak{L};\ j = 1, 2, \ldots n_i)$. The local knot vector set $\mathbf{\Xi}_i$ is generated from successive uniform cell subdivision within the parameter domain Ω, starting from Ω^1. Hence, we obtain nested parameter domains, $\Omega^{i+1} \subset \Omega^i$, and nested local knot vectors, $\mathbf{\Xi}_{i+1} \subset \mathbf{\Xi}_i$. Each knot vector set $\mathbf{\Xi}_i$ defines a set of T-splines $\mathbf{N}^i = \left\{N_j^i\right\}_{j=1}^{n_i}$, which in turn forms a nested T-spline space $\mathcal{N}^i$. T-splines at hierarchy level i can be described by T-splines at hierarchy level j:

$$\mathbf{N}^i = \mathbf{S}^{i,j}\mathbf{N}^j = \prod_{l=i}^{j-1} \mathbf{S}^{l,l+1}\mathbf{N}^{l+1}, \tag{18}$$

with $\mathbf{S}^{l,l+1}$ a subdivision or refinement operator [28], which is solved by Eq. (13) using the local knot vector sets $\mathbf{\Xi}_l$ and $\mathbf{\Xi}_{l+1}$.

The coordinates and weights of anchors on the T-spline mesh $\mathcal{T}^i$ at hierarchy level i are computed as:

$$\mathbf{P}_w^i = \mathbf{S}^{i,1\,\mathrm{T}}\mathbf{P}_w^1 = \left(\prod_{l=1}^{i} \mathbf{S}^{l,l+1}\right)^{\mathrm{T}} \mathbf{P}_w^1 \tag{19}$$

where $\mathbf{P}_w^i$ contains the weighted control points at level i. Each weighted control point is defined as $\mathbf{P}_{w,j}^i = \left(w_j^i x_{1j}^i,\ w_j^i x_{2j}^i,\ w_j^i\right)$. If we consider rational T-spline basis functions, the subdivision operator $\mathbf{S}^{l,l+1}$ in Eq. (18) must be modified as follows [28]:

$$\tilde{S}_{IJ}^{l,l+1} = \frac{w_J^l}{w_J^{l+1}} S_{IJ}^{l,l+1}, \tag{20}$$

where w is the weight in Eq. (19) and $S_{IJ}^{l,l+1}$ is the term in $\mathbf{S}^{l,l+1}$.

We adopt the algorithm of [28] to construct the hierarchical T-spline bases $\mathcal{H}$ or the truncated hierarchical bases $\mathcal{H}_T$. The formulation and the algorithm to determine $\mathcal{H}$ or $\mathcal{H}_T$ have been detailed in [28]. In this contribution, truncated hierarchical bases $\mathcal{H}_T$ are used. The implementation aspects of hierarchical refinement of T-splines for phase-field modeling are outlined in Section 4.3.

4.3. Implementation of adaptive refinement in IGA

As in most calculations of phase-field models, a staggered approach is adopted for the solution of the coupled non-linear problem [10, 23, 37]. In the time-discrete evolution, given the displacement field $\mathbf{u}_n^{(i-1)}$ and phase field $c_n^{(i-1)}$ at time step t_{i-1}, the solution at time t_i is obtained by solving the stationarity conditions for the functional, Eq. (3), under the unilateral constraint $c_n \geq c_n^{(i-1)}$. The

DOI: 10.1002/nme

problem is hence split in a 'displacement' sub-problem and a 'damage' sub-problem. At each time, the two sub-problems are solved iteratively until a convergence criterion has been met.

The 'displacement' sub-problem consists of solving the minimisation problem for $\mathbf{u}_n$ for a given phase field variable c_n:

$$\mathbf{u} = \arg \inf_{\mathbf{u}\in\mathcal{S}_u} \left\{ \int_\Omega a(c_n)\mathcal{W}(\mathbf{u})\, d\Omega - \int_{\Gamma_t} \mathbf{u}\cdot\hat{\mathbf{t}}\mathrm{d}\Gamma \right\} \tag{21}$$

where $\mathcal{S}_u = \left\{\mathbf{u}\in H^1(\Omega),\, \mathbf{u}|\,\Gamma_u = \hat{\mathbf{u}}\right\}$, and $\hat{\mathbf{u}}$ and $\hat{\mathbf{t}}$ represent the prescribed displacements on Γ_u and the tractions on Γ_t, respectively. For the 'phase-field' sub-problem, the solution for c_n is obtained as the minimisation of Eq. (3) for a fixed $\mathbf{u}_n$:

$$c = \arg \inf_{c\in\mathcal{S}_c} \left\{ \int_\Omega a(c)\mathcal{W}(\mathbf{u}_n)\, d\Omega + \frac{\mathcal{G}_0}{\beta\ell_c}\int_\Omega \left(w(c) + \ell_c^4\,\nabla^2 c : \mathbf{C} : \nabla^2 c\right)\, d\Omega \right\} \tag{22}$$

subject to $c \geq c_n^{(i-1)}$, where $\mathcal{S}_c = \left\{c\in H^1(\Omega),\, c|\,\Gamma_c = \hat{c}\right\}$, and $\hat{c}$ denotes the prescribed phase field on Γ_c.

From the minimisation problems in Eqs (21) and (22), we obtain a global system of equations

$$\mathbf{K}\mathbf{U} = \mathbf{F}, \tag{23}$$

where $\mathbf{U}$ includes the nodal degrees of freedom, i.e. the displacement field $\mathbf{u}$ and the phase field c, while $\mathbf{F}$ represents the force vector. With the local refinement strategy of Section 4.1, we first use Bézier extraction to obtain the stiffness matrix of each element in the domain. Then, we solve Eq. (23) to obtain the displacement field $\mathbf{u}$ and the phase field c [26].

For the hierarchical refinement strategy of Section 4.2, we must first derive the stiffness matrix of the active elements at each hierarchy level, without consideration of multi-level blending function interaction [26]. Then, we can assemble the stiffness matrix at each hierarchy level to form the global system of equations $\mathbf{K}$, which is a sparse matrix with the submatrices $\mathbf{K}^i$ along the diagonal. The submatrix $\mathbf{K}^i$ constitutes the stiffness matrix of the active elements at hierarchy level i. To enforce the interaction between the multi-level hierarchical bases $\mathcal{H}$ or $\mathcal{H}_T$ in Eq. (23), a hierarchical subdivision operator $\mathbf{M}_h$ is introduced, which yields the following hierarchical system of equations:

$$\mathbf{K}_h\mathbf{U}_h = \mathbf{F}_h \qquad \text{with} \qquad \mathbf{K}_h = \mathbf{M}_h\mathbf{K}\mathbf{M}_h^{\mathrm{T}} \quad \text{and} \quad \mathbf{F}_h = \mathbf{M}_h\mathbf{F} \tag{24}$$

with $\mathbf{M}_h$ the hierarchical subdivision operator [26, 28]. Solution of Eq. (24) leads to nodal degrees of freedom for the control points which are associated with the hierarchical bases $\mathcal{H}$ or $\mathcal{H}_T$. In a non-linear solution scheme, computing the stiffness matrix $\mathbf{K}$ requires $\mathbf{U}$ rather than $\mathbf{U}_h$ from the previous iteration,

$$\mathbf{U} = \mathbf{M}_h^{\mathrm{T}}\mathbf{U}_h. \tag{25}$$

Below we provide a general procedure for the solution of a phase-field model which employs adaptive isogeometric analysis using local or hierarchical refinement:

- $\mathcal{S}1$ Solve the system of equations to obtain the nodal degrees of freedom collected in $\mathbf{U}$. For adaptive local refinement, Eq. (23) is considered, while for adaptive hierarchical refinement, Eqs (24) and (25) are used.
- $\mathcal{S}2$ Compute the phase field c at the Gauss integration points of each element.
- $\mathcal{S}3$ Mark elements for refinement on the basis of $\mathcal{S}2$, using the criterion that the phase field c in any of the Gauss points exceeds the threshold c_{crit}, in here, $c_{\mathrm{crit}} = 0.2$. For adaptive hierarchical refinement, element marking continues until the highest hierarchy level is attained. For adaptive local refinement, element refinement is carried out until a prescribed smallest element size e_m is reached in the physical domain. For materials with a strongly

DOI: 10.1002/nme

anisotropic surface energy, the crack propagation transiently arrests during loading, which results in an abrupt propagation in a single time step. This could lead to a dependence of the crack path on the underlying meshes [38]. For a strongly anisotropic energy model, the dependence of the numerical solution on the mesh (and also on the algorithm) is due to the fact that small imperfections (due to physics and/or numerical errors) may significantly affect the final solution [38]. To enforce the irreversibility condition, we consider the condition $c \geqslant c_{n-1}$; c_{n-1} denote phase field values from the previous time step (load step).

$\mathcal{S}4$ Refine the marked elements [26]. If no element needs to be refined, stop the calculation and proceed to next step. Otherwise return to $\mathcal{S}1$.

4.4. State vector update after refinement

During refinement, new elements are introduced to accurately capture crack propagation. For non-linear problems, this requires a transfer of the state vector, i.e. the displacements and the phase field, from the previous time t to provide initial values for the new elements at time $t + \Delta t$. The transfer of state vector from coarse elements to finer elements is exact after local and hierarchical refinement [26, 28].

We consider ${}^{t}\mathbf{U}$, which has been obtained at time t. The corresponding T-spline basis function space is ${}^{t}\mathcal{A}$, for instance the LR T-spline space $\mathcal{N}$ for the local refinement of Section 4.1, or the hierarchical T-spline space of Section 4.2. For the next time $t + \Delta t$, certain elements may have been marked for refinement. If so, the basis function space and the control points are updated. We denote the space of basis functions at time $t + \Delta t$ by ${}^{t+\Delta t}\mathcal{A}$.

In a non-linear solution scheme, we need to map the vector ${}^{t}\mathbf{U}$ to produce a new initial vector ${}^{t+\Delta t}_{0}\mathbf{U}$ at time $t + \Delta t$. During element refinement, the mapping of ${}^{t}\mathbf{U}$ to ${}^{t+\Delta t}_{0}\mathbf{U}$ is exact, and is given by [2, 3]:

$$ {}^{t+\Delta t}_{0}\mathbf{U} = \left(\tilde{\mathbf{S}}_t^{\mathrm{T}}\right) {}^{t}\mathbf{U} \tag{26} $$

where $\tilde{\mathbf{S}}_t$ denotes the modified subdivision operator.

For the local refinement strategy of Section 4.1, $\tilde{\mathbf{S}}_t$ is given by:

$$ \tilde{\mathbf{S}}_t = \mathbf{\Gamma}^{\mathrm{T}} \mathbf{S} \mathbf{\Gamma}_r^{-\mathrm{T}} \tag{27} $$

where $\mathbf{\Gamma}$ and $\mathbf{\Gamma}_r$ are diagonal matrices with the scaling weight γ of the T-spline basis functions in the spaces ${}^{t}\mathcal{A}$ and ${}^{t+\Delta t}\mathcal{A}$, respectively. $\mathbf{S}$ denotes the refinement operator between the T-spline basis functions in ${}^{t}\mathcal{A}$ and ${}^{t+\Delta t}\mathcal{A}$. $\mathbf{\Gamma}_r$, $\mathbf{S}$ and $\mathbf{\Gamma}$ are computed using Equation (15).

For the hierarchical refinement in Section 4.2, $\tilde{\mathbf{S}}_t$ is defined between the hierarchy levels [2]. We can obtain the state vector ${}^{t+\Delta t}_{0}\mathbf{U}^{l+1}$ at hierarchy level $l+1$ from the state vector ${}^{t}\mathbf{U}^{l}$ at hierarchy level l through

$$ \tilde{S}^{l,l+1}_{t,IJ} = \begin{cases} S^{l,l+1}_{IJ} & \text{for} \quad N_J^{l+1} \in {}^{t+\Delta t}\mathcal{A}^{l+1} \\ 0 & \text{otherwise} \end{cases} \tag{28} $$

where l is the hierarchy level; $S^{l,l+1}_{IJ}$ denotes the subdivision operator between hierarchy levels l and $l+1$, see Equation (20).

5. EXAMPLES

To assess the performance of the methodology, we present two examples with zigzag crack propagation, namely in a square plate and in a trapezoid specimen, each with a strongly anisotropic surface energy. In the first example, the adaptive refinement techniques (local and hierarchical refinement) are compared numerically, including the crack path, the force-displacement relation and the energy evolution.

In the second example, we only employ the adaptive local refinement technique to trace the crack propagation. We introduce the initial crack as a *discrete* discontinuity in the geometry. A single

DOI: 10.1002/nme

patch is used rather than introducing subdomains with $\mathcal{C}^0$ lines or prescribing the phase-field variable $c = 1$ along the initial crack as often done elsewhere [25]. Indeed, when using isotropic of weakly anisotropic surface energies, a pre-existing crack can be introduced by imposing the condition $c = 1$. However, this is not feasible when a strongly anisotropic surface energy is used because the pre-existing crack can lie in a so-called forbidden direction [20, 24]. Imposing the condition $c = 1$ on such a line poses numerical, but also mathematical and physical issues [23].

In general, T-spline meshes are generated by adaptive local refinement of NURBS meshes [27]. Herein, the initial T-spline mesh is directly defined by NURBS meshes. The corresponding initial local knot vectors $\left(\boldsymbol{\Xi}_1^1, \boldsymbol{\Xi}_1^2\right)$ and the initial control points $\mathbf{P}_1$ are thus directly obtained from the NURBS meshes. In the examples the geometry is modelled with the same polynomial degree $p = 2$ in each parametric direction. For adaptive local refinement, the element-based structured mesh refinement strategy is employed. For adaptive hierarchical refinement, the truncated hierarchical bases are employed to describe the geometry of domain and also to approximate the solution space.

With a suitable rescaling of the loading [39], we can set Young's modulus $E = 1$ and the surface energy $\mathcal{G}_0 = 1$ to describe all the experiments. Poisson's ratio is set $\nu = 0.3$. Here, we consider a strongly anisotropic surface energy of the form $\mathcal{G}_c(\theta) = \sqrt[4]{1 + 0.8\cos 4\,(\theta + \theta_0)}$ by setting $C_{1111} = 1.8$, $C_{1122} = -1.7$ and $C_{1212} = 0.15$ and then applying a standard transformation for the rotation of $\mathbf{C}$ by an angle θ_0 [23].

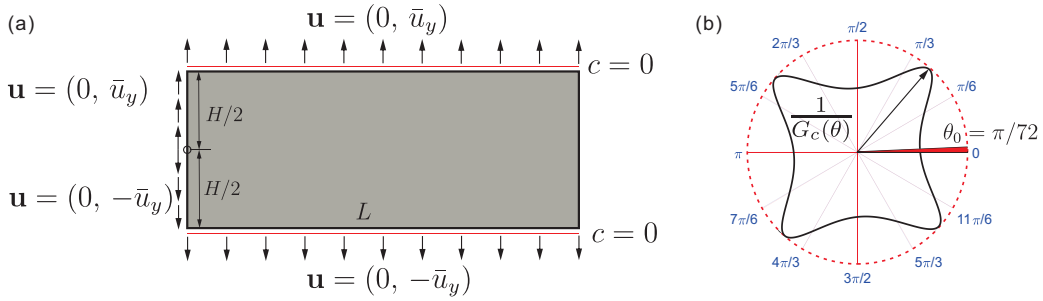

Figure 6. (a) Geometry and boundary conditions for a square plate. $c = 0$ is imposed on the upper and lower boundaries; (b) polar plot of the reciprocal surface energy $1/\mathcal{G}_c(\theta)$, with $\mathcal{G}_c(\theta) = \sqrt[4]{1 + 0.8\cos 4\,(\theta + \pi/72)}$.

5.1. Zigzag crack propagation in a square plate

We consider a unit rectangular domain under tension loads. Figure 6(a) shows the geometry and the boundary conditions. The width of the plate is given as the unit length $L = 1$ with a height $H = 0.4L$. Plane-stress conditions are assumed. The rotation of the fourth-order tensor $\mathbf{C}$ is given by $\theta_0 = \pi/72$, see Figure 6(b). The internal length scale $\ell_c = 0.02$. We set the smallest element size $e_m = l/5$ for adaptive local refinement, which corresponds to a hierarchy of 3 levels to construct truncated hierarchical bases. The initial meshes for the global, adaptive local and hierarchical refinement are given in Figure 8. For the initial meshes of adaptive refinement, the left, top and bottom boundaries are discretised in order to match the boundary conditions in the case of global refinement. For global refinement, the reference solution, 200×100 elements are employed to discretise the domain.

The computed load-displacement curve, and the elastic and surface energies are shown in Figure 7. A good agreement is obtained between the solutions of global and adaptive refinement. The first jump in the force and the energies relates to the re-initiation of the crack associated with an add-crack of finite length appearing in a single time step, see Figure 8(right). The second jump and third jump (not well visible due to the small values) are manifestations of unstable crack propagation at each kink [23]. These jumps are consistent with theoretical analyses [40], which show that a crack kinking is associated with a jump in time and space of the propagating crack.

The predicted crack paths for the adaptive mesh and for the uniformly refined mesh are shown in Figure 8. The solutions produce similar crack patterns. The adaptive algorithm well captures the

DOI: 10.1002/nme

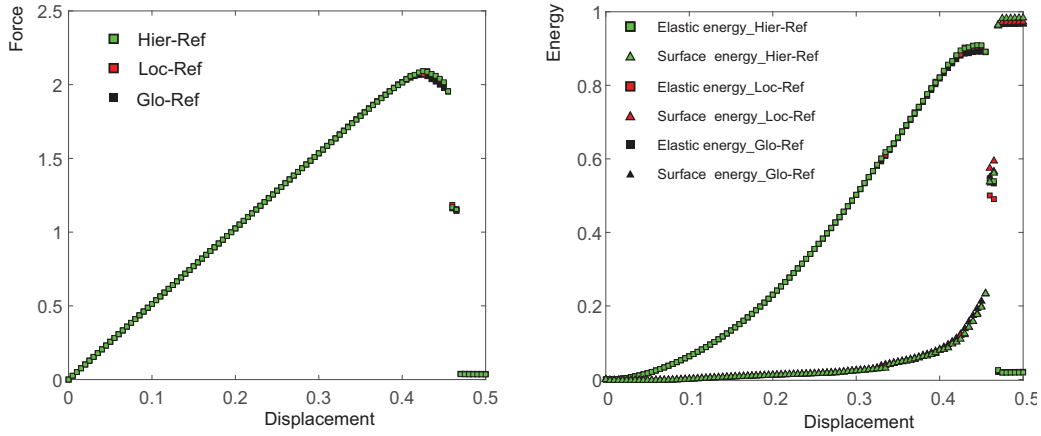

Figure 7. Load-displacement curve and evolution of the elastic and surface energies. The force is obtained by summation of loads in the y-direction along the top boundary. "Hier-Ref" represents the results of adaptive hierarchical refinement and "Loc-Ref" denotes those of adaptive local refinement, while "Glo-Ref" stands for those of global refinement, which are taken as the reference solution.

zigzag behaviour of crack propagation. A slight difference occurs between the crack paths due to the dependence on the underlying meshes [38], see Section 4.3.

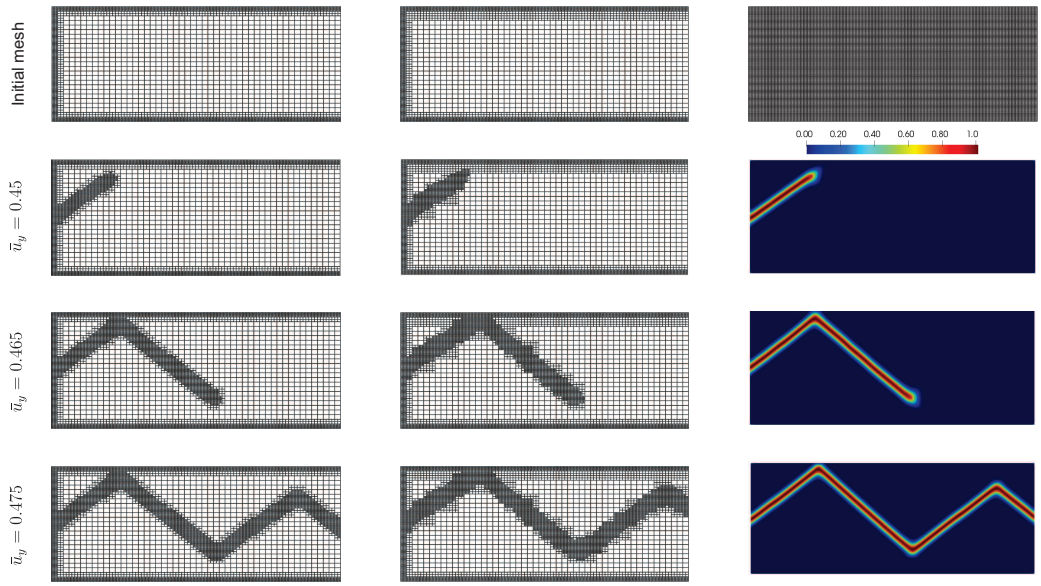

Figure 8. Meshes for the hierarchical (left) and local (middle) refinement, and the phase field c (right) on a globally refined mesh at different load steps.

5.2. Zigzag crack propagation in a curved plate

In this section, we consider a curved plate under tension loading. The geometry and boundary conditions are shown in Figure 9(a). The width of the plate is given as the unit length $L = 1$. The domain is initially discretised by NURBS with a polynomial degree $p = 3$ and $q = 1$ respectively in the horizontal and vertical direction. The knot vectors are given as $\boldsymbol{\Xi}^1 = [0, 0, 0, 0, 1/3, 2/3, 1, 1, 1, 1]$ and $\boldsymbol{\Xi}^2 = [0, 0, 0, 1, 1, 1]$. The coordinates of control points $\mathbf{P}$ are given in Figure 9(b). In this example, we consider NURBS with polynomial degrees $p = 3$ and $q = 3$. The knot vector and the control points are updated by order elevation from initial NURBS.

DOI: 10.1002/nme

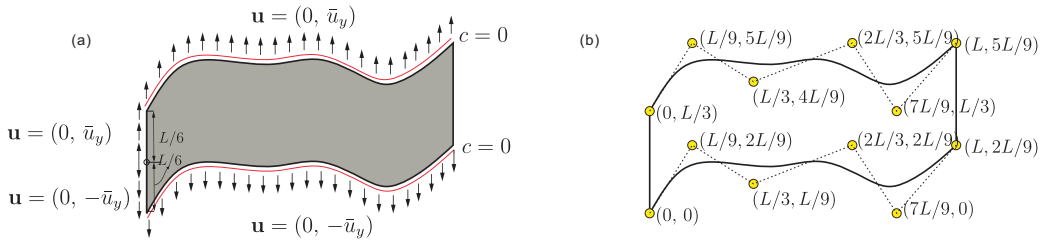

Figure 9. (a) Geometry and boundary conditions for a curved specimen. $c = 0$ is imposed on the upper and lower boundaries; (b) Bézier physical mesh and control points, all the weights of control points are $w = 1$.

Plane-stress conditions are assumed. The rotation of the fourth-order tensor $\mathbf{C}$ is given by $\theta_0 = \pi/72$, see Figure 6(b). The internal length scale $\ell_c = 0.02$. In this example, we will employ the adaptive hierarchical refinement to trace the crack propagation. To construct truncated hierarchical bases, we consider the smallest element size $e_m = l/5$, which corresponds to a hierarchy of 3 levels. The initial meshes for the global and adaptive hierarchical refinement are given in Figure 11. For global refinement, the reference solution, 300×80 elements are employed to discretise the domain.

As expected, in Figure 10, a good agreement is obtained for the load-displacement curve, and the elastic and surface energies in the case of global and adaptive refinement. The jumps in the figure relates to the re-initiation of crack and unstable crack propagation in a single time step, see Figure 11(bottom), which are consistent with theoretical analyses [40]. Similar crack patterns are observed for the the adaptive refinement and for the global refinement, see Figure 11. The crack path initiates from the left side of the plate with an angle similar to that in Figure 8 due to the restriction of forbidden crack directions [23]. For the crack propagation direction, it has been suggested that the underlying crack path selection is dictated by the Generalized Maximum Energy Release Rate criterion (GMERR) [23], which postulates that the crack propagate in a direction given by the angle θ such that $\mathcal{G}(\theta)/\mathcal{G}_c(\theta)$ attains a maximum among all $\theta \in [-\pi, \pi]$. Checking the crack propagation direction explicitly requires the computation of $\mathcal{G}(\theta)$ at each time step using the Leblond expansion [41], i.e. computing the stress intensity factors (SIFs). However, the computation of SIFs is nontrivial and requires the calculation of a path-dependent integral [42].

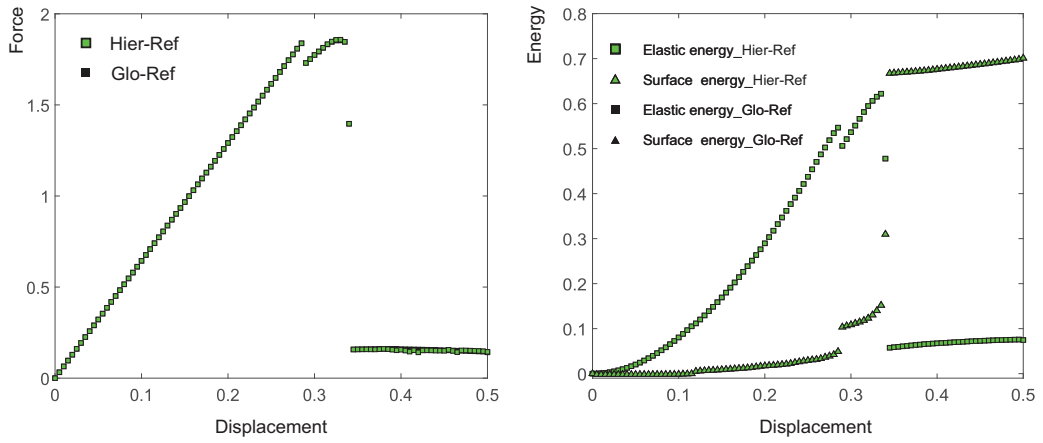

Figure 10. Load-displacement response and evolution of the elastic and the surface energies. The force is obtained by summation of the loads in the y-direction along the top boundary. "Hier-Ref" denotes results of the adaptive local refinement, while "Glo-Ref" stands for those of global refinement.

5.3. Zigzag crack propagation in a trapezoid specimen

We now introduce an initial crack as a discrete discontinuity in the geometry instead of introducing subdomains or prescribing phase field values $c = 1$. The adaptive local refinement strategy is

DOI: 10.1002/nme

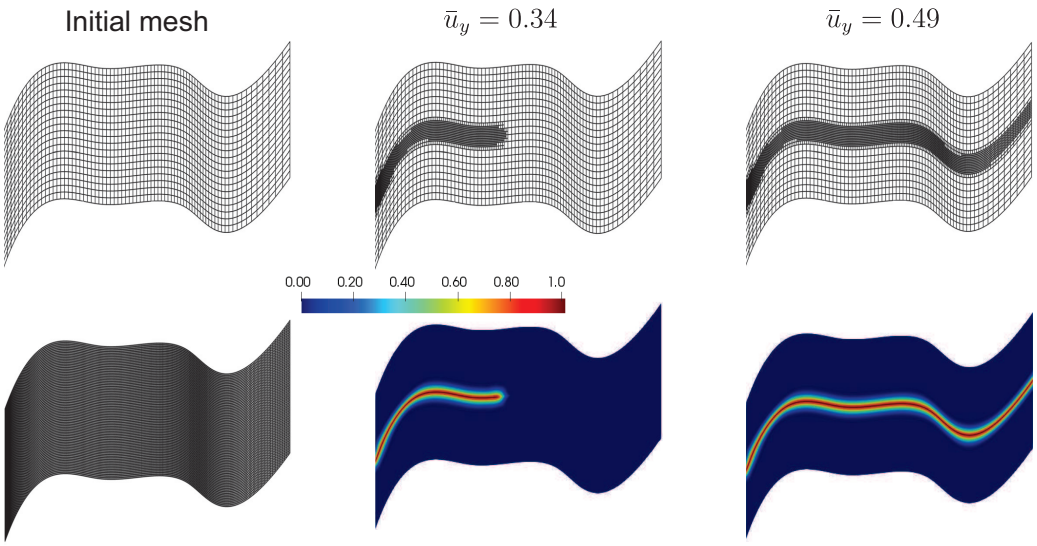

Figure 11. Meshes for the hierarchical (top) refinement, and the phase field c (bottom) for a globally refined mesh at different load steps.

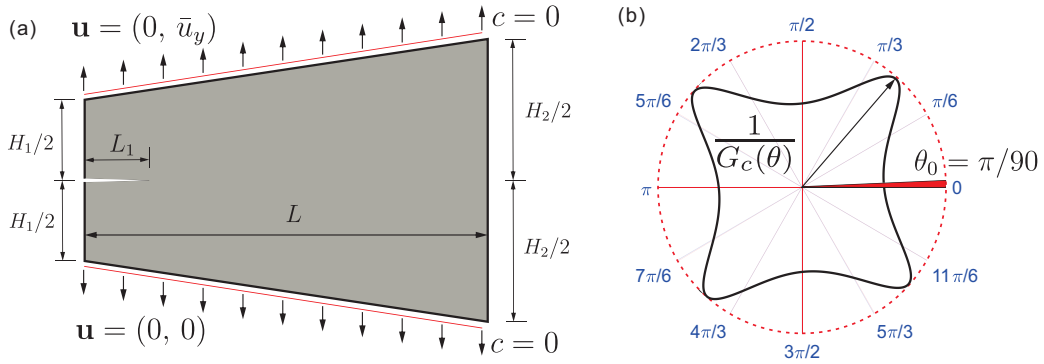

Figure 12. (a) Geometry and boundary conditions for a trapezoid specimen. $c = 0$ is imposed on the upper and lower boundaries; (b) polar plot of the reciprocal surface energy $1/\mathcal{G}_c(\theta)$, with $\mathcal{G}_c(\theta) = \sqrt[4]{1 + 0.8\cos 4\,(\theta + \pi/90)}$.

employed. The geometry of the specimen has a trapezoidal shape and is pre-cracked, see Figure 12(a), which also shows the Dirichlet boundary conditions, with $c = 0$ for the phase field and prescribed displacements $\bar{u}_y$ on the top and bottom boundaries. The polar plot of the reciprocal surface energy $1/\mathcal{G}_c(\theta)$ is shown in Figure 12(b). The rotation of $\mathbf{C}$ is given by $\theta_0 = \pi/90$. The width of the plate is given as $L = 1$ with heights $H_1 = 0.4L$ and $H_2 = 0.8L$, respectively. Plane-stress conditions are assumed.

The initial crack is placed in the centre line with a length $L_1 = 0.16L$. Basically, one can introduce several subdomains separated by $\mathcal{C}^0$ lines or prescribe phase-field values $c = 1$ along the initial crack [25] to represent an initial crack in the isogeometric analysis. However, using subdomains with $\mathcal{C}^0$ lines is detrimental for the higher-order continuity of the splines interpolation. It actually degenerates into standard finite elements with several 'macroelements'. Moreover, prescribing $c = 1$ directly is not allowed in models with a strongly anisotropic surface energy. For these reasons we will introduce the initial crack as a discrete discontinuity in the geometry. This is done by meshline insertions in the locally refined T-mesh, which yields discontinuous basis functions [3]. By repeating meshline insertions in the parameter space, the order of the interpolation can be decreased locally, till $\mathcal{C}^{-1}$ continuity, and a discontinuity results in the physical space. We will use the example of Figure 13 to illustrate the concept. Figure 13(a-left) is the initial T-mesh used to describe the trapezoid

DOI: 10.1002/nme

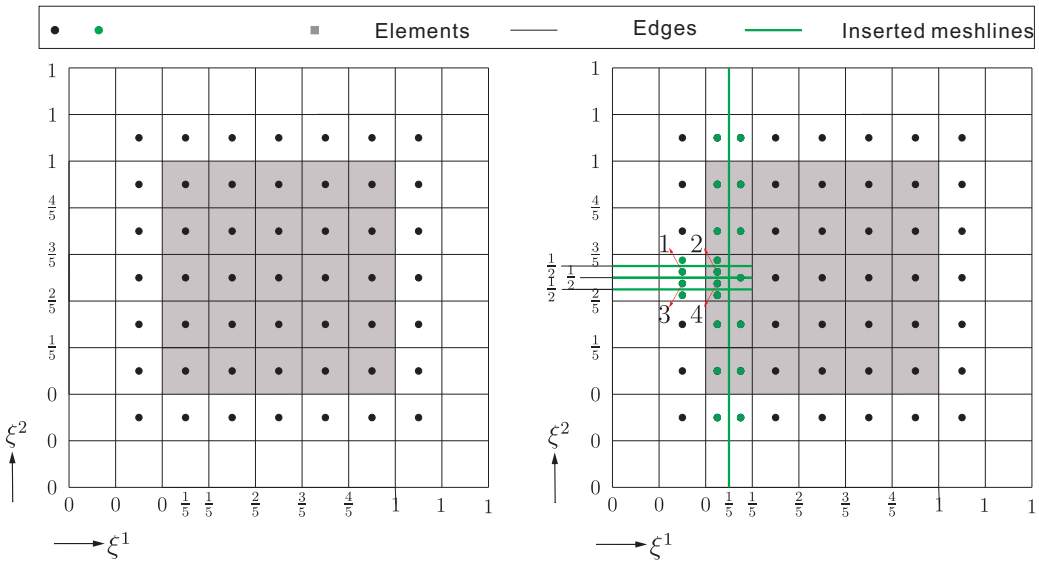

(a) Ω in the index and parameter domain before (left) and after (right) inserting the initial crack

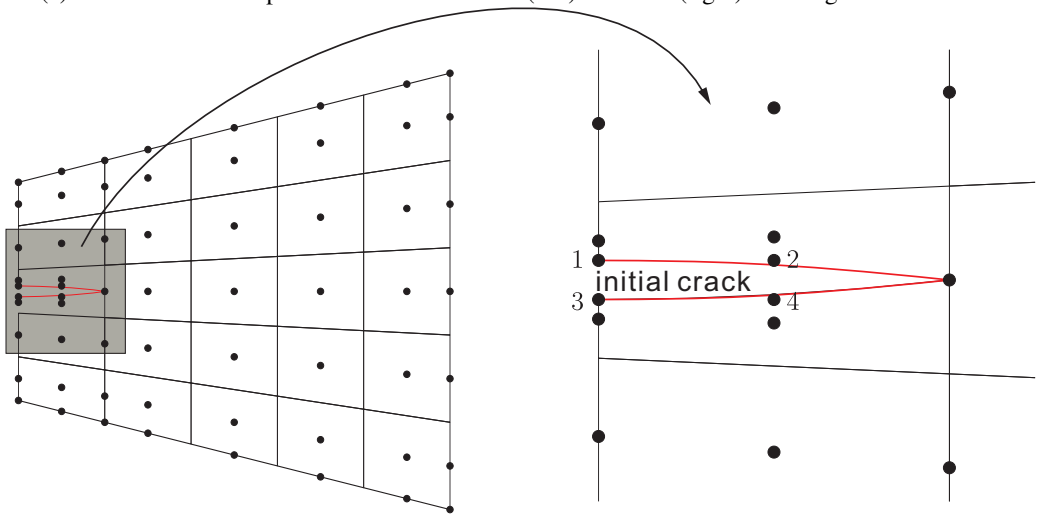

(b) Ω in the physical domain after inserting the initial crack

Figure 13. Trapezoid plate Ω in the index, parameter and physical domains before and after inserting the initial crack. In (b), a shift is applied to control points $1, \cdots, 4$ to better visualise the initial crack.

plate. In order to introduce the initial crack in the middle plane we insert the green meshlines in the ξ^1 parametric direction, see Figure 13(a-right) [3]. Figure 13(b) represents the trapezoid plate in the physical domain after meshline insertions. Due to the discontinuity, the coordinates of the control points $1,\ 2$ equal those of control points $3,\ 4$, Figure 13(a-right). To better visualise the discontinuity in Figure 13(b) a shift $\left(\delta^1, \delta^2\right)$ has been applied to control points $1, \cdots, 4$:

$$\left(\delta_1^1, \delta_1^2\right) = (0, 0.01) \quad \left(\delta_2^1, \delta_2^2\right) = (0, 0.01) \quad \left(\delta_3^1, \delta_3^2\right) = (0, -0.01) \quad \left(\delta_4^1, \delta_4^2\right) = (0, -0.01) \quad (29)$$

Figure 13(b) illustrates a crack passing through the middle plane. Figure 13(b-left) is the diagram of the trapezoid plate Ω, while Figure 13(b-right) shows the enlargement of the initial crack.

The evolution of external loads, the elastic and the surface energies as a function of the displacement $\bar{u}_y$ is shown in Figure 14. The results of the adaptive local refinement agree well with those of the global refinement. In the figure, the first jump in the force and the energy reflects the initiation of the crack, see the first crack kink. The second and the third jump correspond to

DOI: 10.1002/nme

unstable crack propagation at a kink. Figure 15 presents the crack paths which stem from adaptive refinement and global refinement. The adaptive refinement well captures the evolution of the phase field. The kinking of the propagating crack is also illustrated.

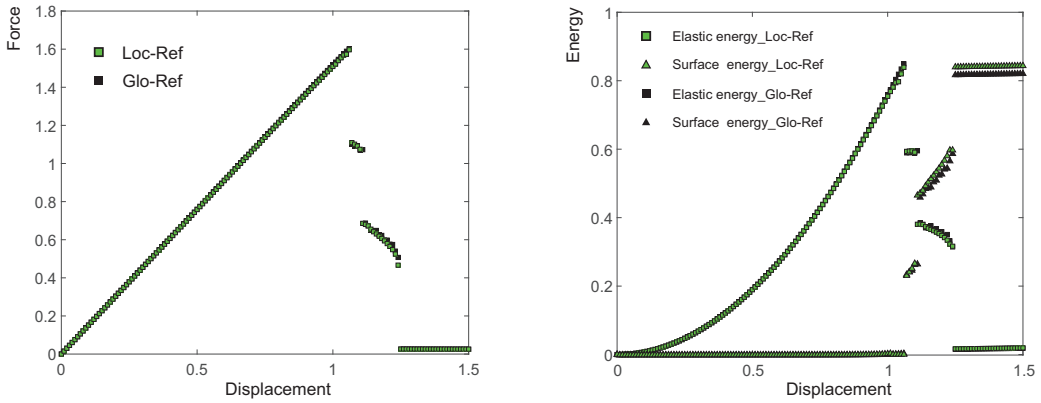

Figure 14. Load-displacement response and evolution of the elastic and the surface energies. The force is obtained by summation of the loads in the y-direction along the top boundary. "Loc-Ref" denotes results of the adaptive local refinement, while "Glo-Ref" stands for those of global refinement.

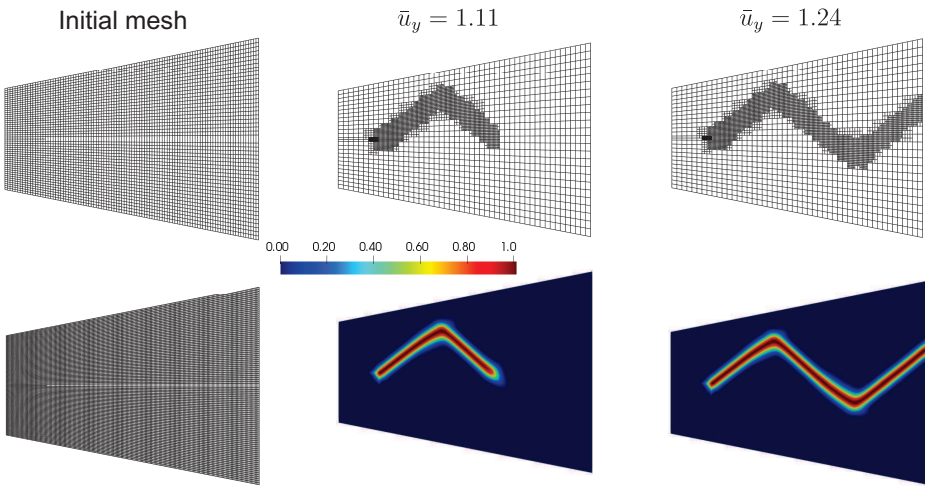

Figure 15. Meshes for the local (top) refinement, and the phase field c (bottom) for a globally refined mesh at different load steps.

6. CONCLUDING REMARKS

Higher-order phase-field models for fracture have been considered to investigate crack propagation in materials with a strongly anisotropic surface energy. In these models, the existence of higher-order derivatives of the phase-field variable in the energy functional necessitates $\mathcal{C}^1$ continuous basis functions. Herein, we have employed the T-splines as the basis functions. To accurately capture the crack topology, a small value of the internal length is preferred. This, however, requires fine discretisatons. This requirement is mitigated by the use of T-splines, which are more accurate than Lagrangian polynomials, and a further improvement in efficiency is obtained by locally refining the areas where the crack propagates. We have considered hierarchical as well as local refinement strategies. Using Bézier extraction, standard finite element data structures can still be used. Algorithms have been provided for both refinement techniques.

DOI: 10.1002/nme

Three examples have been studied numerically and show that for adaptive refinement, the crack pattern, the force-displacement relation and the energy evolution well match those obtained using a globally refined mesh. The computation time is reduced by 30% $\sim$ 50% for the cases studied. Finally, the technology makes it possible to introduce an initial crack as a discrete discontinuity in the geometry, which by-passes the need to reduce continuity in isogeometric analysis or to prescribe phase-field values $c = 1$ in the domain.

ACKNOWLEDGEMENT

Financial support from the European Research Council (ERC Advanced Grant 664734 PoroFrac) is gratefully acknowledged.

CONFLICT OF INTEREST

The authors declare that there is no conflict of interest regarding the publication of this paper.

REFERENCES

[1] de Borst R, Remmers JJC, Needleman A, Abellan MA. Discrete vs smeared crack models for concrete fracture: bridging the gap. *International Journal for Numerical and Analytical Methods in Geomechanics* 2004; **28**:583–607.

[2] Chen L, Lingen EJ, de Borst R. Adaptive hierarchical refinement of NURBS in cohesive fracture analysis. *International Journal for Numerical Methods in Engineering* 2017; **112**:2151–2173.

[3] Chen L, Verhoosel CV, de Borst R. Discrete fracture analysis using locally refined T-splines. *International Journal for Numerical Methods in Engineering* 2018; **116**:117–140.

[4] Chen L, de Borst R. Cohesive fracture analysis using powell-sabin B-splines. *International Journal for Numerical and Analytical Methods in Geomechanics* 2019; **43**:625–640.

[5] Chen L, Li B, de Borst R. Energy conservation during remeshing in the analysis of dynamic fracture. *International Journal for Numerical Methods in Engineering* 2019; **120**:433–446.

[6] de Borst R, Gutiérrez MA. A unified framework for concrete damage and fracture models including size effects. *International Journal of Fracture* 1999; **95**:261–277.

[7] Peerlings RHJ, de Borst R, Brekelmans WAM, de Vree HPJ. Gradient-enhanced damage for quasi-brittle materials. *International Journal for Numerical Methods in Engineering* 1996; **39**:3391–3403.

[8] Francfort GA, Marigo JJ. Revisiting brittle fracture as an energy minimization problem. *Journal of the Mechanics and Physics of Solids* 1998; **46**:1319–1342.

[9] Bourdin B, Francfort GA, Marigo JJ. The variational approach to fracture. *Journal of Elasticity* 2008; **91**:5–148.

[10] Miehe C, Hofacker M, Welschinger F. A phase field model for rate-independent crack propagation: Robust algorithmic implementation based on operator splits. *Computer Methods in Applied Mechanics and Engineering* 2010; **199**:2765–2778.

[11] Miehe C, Welschinger F, Hofacker M. Thermodynamically consistent phase-field models of fracture: Variational principles and multi-field FE implementations. *International Journal for Numerical Methods in Engineering* 2010; **83**:1273–1311.

[12] de Borst R, Verhoosel CV. Gradient damage *vs* phase-field approaches for fracture: Similarities and differences. *Computer Methods in Applied Mechanics and Engineering* 2016; **312**:78–94.

[13] Bourdin B, Francfort GA, Marigo JJ. Numerical experiments in revisited brittle fracture. *Journal of the Mechanics and Physics of Solids* 2000; **48**:797–826.

[14] Hesch C, Schuß S, Dittmann M, Franke M, Weinberg K. Isogeometric analysis and hierarchical refinement for higher-order phase-field models. *Computer Methods in Applied Mechanics and Engineering* 2016; **303**:185–207.

[15] Wu JY. A unified phase-field theory for the mechanics of damage and quasi-brittle failure. *Journal of the Mechanics and Physics of Solids* 2017; **103**:72–99.

[16] Li B, Millán D, Torres-Sánchez A, Roman B, Arroyo M. A variational model of fracture for tearing brittle thin sheets. *Journal of the Mechanics and Physics of Solids* 2018; **119**:334–348.

[17] Judt PO, Ricoeur A, Linek G. Crack path prediction in rolled aluminum plates with fracture toughness orthotropy and experimental validation. *Engineering Fracture Mechanics* 2015; **138**:33–48.

[18] Ibarra A, Roman B, Melo F. The tearing path in a thin anisotropic sheet from two pulling points: Wulff's view. *Soft Matter* 2016; **12**:5979–5985.

[19] Gao Y, Liu Z, Zeng Q, Wang T, Zhuang Z, Hwang KC. Theoretical and numerical prediction of crack path in the material with anisotropic fracture toughness. *Engineering Fracture Mechanics* 2017; **180**:330–347.

[20] Li B, Peco C, Millán D, Arias I, Arroyo M. Phase-field modeling and simulation of fracture in brittle materials with strongly anisotropic surface energy. *International Journal for Numerical Methods in Engineering* 2015; **102**:711–727.

[21] Teichtmeister S, Kienle D, Aldakheel F, Keip MA. Phase field modeling of fracture in anisotropic brittle solids. *International Journal of Non-Linear Mechanics* 2017; **97**:1–21.

[22] Kakouris E, Triantafyllou S. Material point method for crack propagation in anisotropic media: a phase field approach. *Archive of Applied Mechanics* 2018; **88**:287–316.

[23] Li B, Maurini C. Crack kinking in a variational phase-field model of brittle fracture with strongly anisotropic surface energy. *Journal of the Mechanics and Physics of Solids* 2019; **125**:502–522.

[24] Takei A, Roman B, Bico J, Hamm E, Melo F. Forbidden directions for the fracture of thin anisotropic sheets: an analogy with the Wulff plot. *Physical Review Letters* 2013; **110**:144 301.

[25] Borden MJ, Verhoosel CV, Scott MA, Hughes TJR, Landis CM. A phase-field description of dynamic brittle fracture. *Computer Methods in Applied Mechanics and Engineering* 2012; **217-220**:77–95.

[26] de Borst R, Chen L. The role of Bézier extraction in adaptive isogeometric analysis: Local refinement and hierarchical refinement. *International Journal for Numerical Methods in Engineering* 2018; **113**:999–1019.

[27] Chen L, de Borst R. Locally refined T-splines. *International Journal for Numerical Methods in Engineering* 2018; **114**:637–659.

[28] Chen L, de Borst R. Adaptive refinement of hierarchical T-splines. *Computer Methods in Applied Mechanics and Engineering* 2018; **337**:220–245.

[29] Chen L. Three-dimensional Greens function for an anisotropic multi-layered half-space. *Computational Mechanics* 2015; **56**:795–814.

DOI: 10.1002/nme

[30] Bazilevs Y, Calo VM, Cottrell JA, Evans JA, Hughes TJR, Lipton S, Scott MA, Sederberg TW. Isogeometric analysis using T-splines. *Computer Methods in Applied Mechanics and Engineering* 2010; **199**:229–263.

[31] Dörfel MR, Jüttler B, Simeon B. Adaptive isogeometric analysis by local h-refinement with T-splines. *Computer Methods in Applied Mechanics and Engineering* 2010; **199**:264–275.

[32] Evans EJ, Scott MA, Li X, Thomas DC. Hierarchical T-splines: Analysis-suitability, Bézier extraction, and application as an adaptive basis for isogeometric analysis. *Computer Methods in Applied Mechanics and Engineering* 2015; **284**:1–20.

[33] Johannessen KA, Kvamsdal T, Dokken T. Isogeometric analysis using LR B-splines. *Computer Methods in Applied Mechanics and Engineering* 2014; **269**:471–514.

[34] Forsey DR, Bartels RH. Hierarchical B-spline refinement. *ACM Siggraph Computer Graphics* 1988; **22**:205–212.

[35] Kolo I, Chen L, de Borst R. Strain-gradient elasticity and gradient-dependent plasticity with hierarchical refinement of NURBS. *Finite Elements in Analysis and Design* 2019; **163**:31–43.

[36] Giannelli C, Jüttler B, Speleers H. THB-splines: The truncated basis for hierarchical splines. *Computer Aided Geometric Design* 2012; **29**:485–498.

[37] Bourdin B. Numerical implementation of the variational formulation for quasi-static brittle fracture. *Interfaces and Free Boundaries* 2007; **9**:411–430.

[38] Pham K, Amor H, Marigo JJ, Maurini C. Gradient damage models and their use to approximate brittle fracture. *International Journal of Damage Mechanics* 2011; **20**:618–652.

[39] Farrell P, Maurini C. Linear and nonlinear solvers for variational phase-field models of brittle fracture. *International Journal for Numerical Methods in Engineering* 2017; **109**:648–667.

[40] Chambolle A, Francfort GA, Marigo JJ. When and how do cracks propagate? *Journal of the Mechanics and Physics of Solids* 2009; **57**:1614–1622.

[41] Amestoy M, Leblond JB. Crack paths in plane situationsII. Detailed form of the expansion of the stress intensity factors. *International Journal of Solids and Structures* 1992; **29**:465–501.

[42] Wang Y, Waisman H, Harari I. Direct evaluation of stress intensity factors for curved cracks using Irwin's integral and XFEM with high-order enrichment functions. *International Journal for Numerical Methods in Engineering* 2017; **112**:629–654.

DOI: 10.1002/nme